

Pmt4 recognizes two separate acceptor sites to O-mannosylate in the S/T-rich regions of substrate proteins

Received: 21 May 2025

Minge Du^{1,2}, Zuanning Yuan^{1,2}, Amanda Kovach¹, Meinan Lyu¹ & Huilin Li¹ 

Accepted: 25 September 2025

Published online: 04 November 2025

 Check for updates

Protein O-mannosyltransferases (PMTs) add mannose to serine/threonine (S/T)-rich proteins in the endoplasmic reticulum, facilitating proper folding and trafficking through the secretory pathway. These enzymes share a conserved architecture that includes a large transmembrane domain housing the catalytic pocket and a luminal β -trefoil-folded MIR domain. Although S/T-rich regions in acceptor proteins are generally disordered, it remains unclear how PMTs selectively target these regions over other intrinsically disordered sequences. Here, using cryo-EM and X-ray crystallography, we demonstrate that the *Saccharomyces cerevisiae* Pmt4 dimer recognizes an S/T-rich peptide at two distinct sites. A groove above the catalytic pocket in the transmembrane domain binds the mannose-accepting S/T site, while the luminal MIR domain engages an S/T-X-S/T motif. Notably, the substrate peptide is simultaneously bound by the catalytic pocket of one Pmt4 protomer and the MIR domain of the other, revealing an unexpected cooperative dual substrate recognition mechanism. This mechanism likely underpins the invariant dimeric architecture observed in all PMT family members.

Protein O-mannosylation is an essential posttranslational modification conserved across eukaryotes and certain bacteria, playing a pivotal role in protein folding, stability, and intercellular communication^{1,2}. Catalyzed by protein O-mannosyltransferases (PMTs in yeast and POMTs in mammals)^{3,4}, this process transfers mannose from dolichol phosphate-activated mannose (Dol-P-Man) to serine or threonine residues on target proteins^{5–7}. This modification is crucial not only for the quality control of unfolded proteins but also for regulating receptor recycling, immune responses, and overall cellular homeostasis⁸. Alterations in O-mannosylation have been implicated in a range of human diseases⁹. For example, mutations in the POMT1–POMT2 complex cause congenital muscular dystrophies such as Walker–Warburg syndrome and muscle–eye–brain disease^{10,11}. Defective O-mannosylation has also been linked to cancer metastasis and viral entry, underscoring its broad clinical significance^{12,13}. In addition to the PMT/POMT, proteins can also be O-mannosylated by the TMTC1–4 enzymes^{14,15} or C-mannosylated to a tryptophan by the

DPY19 family of enzymes^{16,17}. These enzymes all belong to the evolutionarily conserved GT-C family of protein glycosyltransferases^{18,19}.

In fungal pathogens, impaired O-mannosylation disrupts cell wall integrity and morphogenesis²⁰, leading to attenuated virulence²¹. Similarly, in plant pathogens like *Ustilago maydis*²², aberrant PMT activity undermines proper appressorium formation and host invasion, thereby contributing to disease development^{20,22,23}. Together, these findings highlight the evolutionary conservation of protein O-mannosylation and its critical role in maintaining cellular function, with far-reaching implications for organismal health across different kingdoms.

While the substrate recognition and catalytic mechanisms of protein N-glycosylation are well characterized^{24–26}, those governing protein O-mannosylation remain poorly understood. In *Saccharomyces cerevisiae*, six PMT proteins are classified into three subfamilies²⁷: PMT1 (comprising Pmt1 and Pmt5), PMT2 (Pmt2, Pmt3, and Pmt6), and PMT4 (Pmt4), each displaying unique substrate specificity properties^{28,29}. Notably, Pmt1 and Pmt2 form heterodimers to

¹Department of Structural Biology, Van Andel Institute, Grand Rapids, MI, USA. ²These authors contributed equally: Minge Du, Zuanning Yuan.

 e-mail: Huilin.Li@vai.org

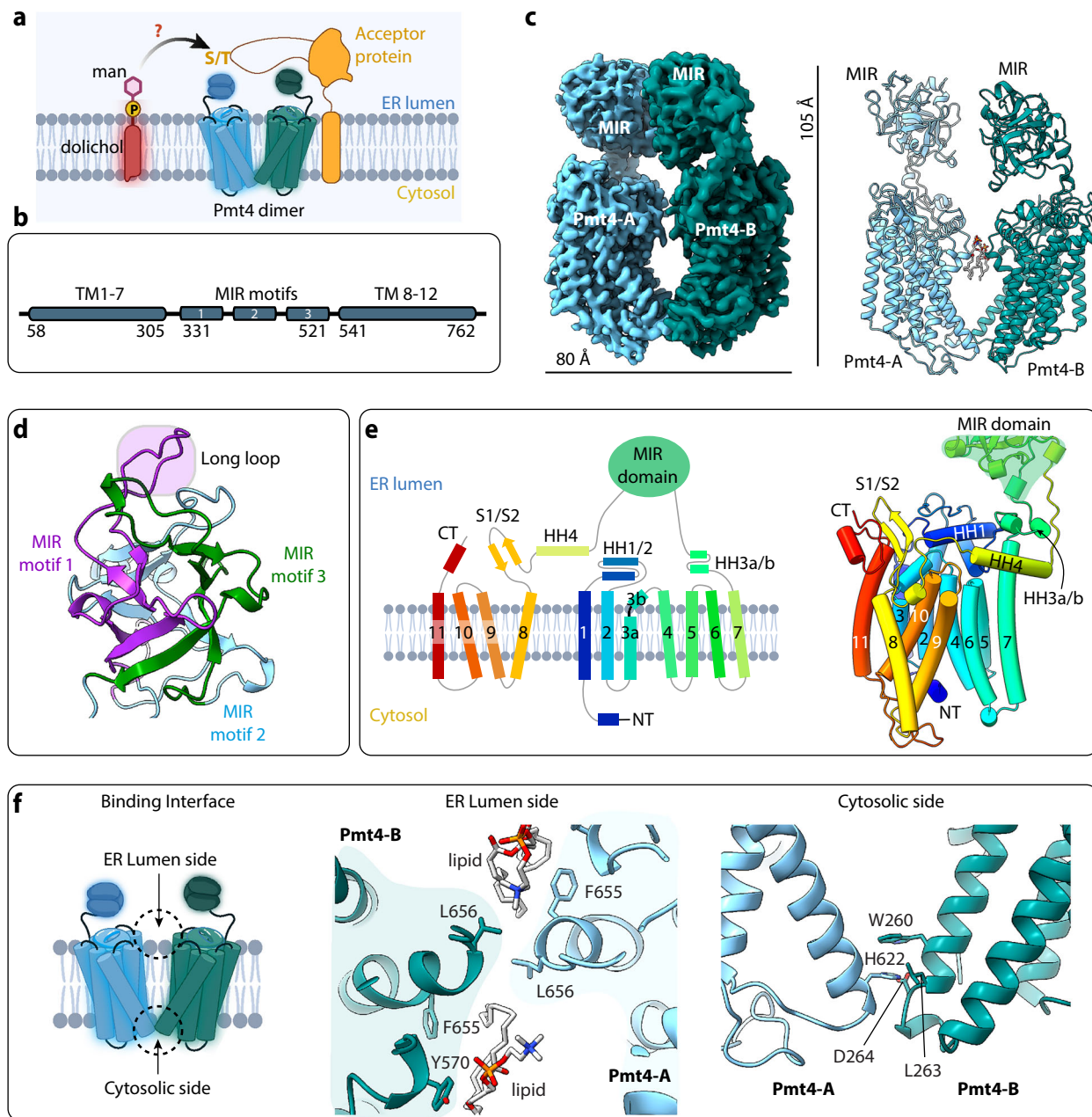


Fig. 1 | Structure of the Pmt4 dimer. **a** Sketch of Pmt4-mediated mannosylation of a nascent protein (Created in BioRender, Fontana, T). The question mark indicates the unknown molecular mechanism. Created in BioRender. <https://BioRender.com/wdqk9wc>. **b** Domain architecture. **c** Cryo-EM map processed by EMReady (left) and atomic model in cartoon view (right) of the apo Pmt4 dimer. Protomers A and B are in cyan and teal, respectively. **d** Crystal structure of the MIR domain. **e** Ribbon

diagram of Pmt4 topology, with transmembrane helices, horizontal helices (HH), and β-strands (S1/S2) numbered and colored in a rainbow scheme. The MIR domain is depicted as a green disk. The HH1-4 and S1-2 form the catalytic pocket with a substrate-peptide-binding groove. **f** Two contacts at luminal and cytosolic sides between Pmt4 A and B. Created in BioRender. <https://BioRender.com/wdqk9wc>.

modify substrates such as Aga2, Bar1, Cts1, Kre9, and Pir2³⁰, whereas Pmt4 forms homodimers that preferentially modify proteins with serine/threonine (S/T)-rich regions, including Ccw5, Axl2, Fus1, Gas1, and Kex2³¹. This functional divergence underscores the specificity within the PMT family and their distinct roles in cellular processes. Recent structural studies on the Pmt1–Pmt2 complex have revealed an architecture featuring an 11-transmembrane helix bundle and a luminal MIR domain³². Furthermore, crystal structures of the MIR domains from Pmt2 and Pmt3 suggest the presence of mannose-binding sites within these regions³³. Despite these advances, several studies have highlighted that PMT4's substrate recognition is far more complex, relying on determinants beyond a simple linear peptide sequence, with

membrane association playing a critical role (Fig. 1a)³⁴. It remains unclear whether PMT enzymes have evolved specific mechanisms to recognize intrinsically disordered S/T-rich regions or if these regions merely serve as general targets for mannosylation^{35,36}. Crucially, high-resolution structural information for PMT4 is conspicuously absent, and its working mechanism remains elusive. This gap in our structural and mechanistic understanding of PMT4 underscores the need for further research to elucidate its precise role in O-mannosylation, which may ultimately reveal novel targets for therapeutic intervention in diseases linked to aberrant glycosylation.

In this work, we report the structures of the *S. cerevisiae* Pmt4 dimer alone and in complex with an acceptor peptide. We show that the MIR

domain of one Pmt4 subunit recognizes a S/T-X-S/T motif while the MIR domain of the other Pmt4 subunit recognizes the acceptor residue S/T. Therefore, the Pmt4 dimer has evolved a trans-recognition mechanism that detects the coincidence of these two acceptor features to ensure mannosylation only to the S/T-rich region of target proteins.

Results and discussion

Overall structure of the Pmt4 dimer

We added a 3 \times FLAG purification tag at the carboxyl terminus of Pmt4 and produced the enzyme in baker's yeast (Supplementary Fig. 1a, b). Cryo-EM analysis of the as-purified Pmt4 resulted in a 3D map at an average resolution of 3.9 Å (Supplementary Figs. 1c, 2). As expected, Pmt4 assembled as a dimer (Fig. 1a–c). The 3D map in the transmembrane regions had good main chain connectivity and side chain density for atomic modeling. However, the two luminal MIR domains had weak density, indicative of partial mobility. To remediate the modeling problem in the MIR domain, we determined the crystal structure of the truncated Pmt4 MIR domain (amino acids 327 to 522) at 1.65 Å resolution and then rigid-body docked the MIR domain atomic model into the low-resolution MIR densities to derive a near full-length atomic model for the Pmt4 dimer, missing only the amino-terminal 34 residues (Fig. 1c, d).

The Pmt4 dimer is pseudo twofold symmetric, with an overall size of 105 \times 80 \times 67 Å³ (Fig. 1c). The overall architecture can be divided into the top MIR domains in the lumen and the large TMD regions. The Pmt4 MIR domain has the expected β -trefoil fold comprised of four β -strands and one short α -helix (Fig. 1d). While the overall fold of Pmt4 MIR is similar to that of Pmt1–Pmt2, there are two distinctions: First, the two MIR domains in Pmt1–Pmt2 tilt toward their opposing subunits and have a largely symmetrical arrangement, but in the Pmt4 dimer, the two MIR domains are asymmetrically arranged, with the Pmt4-A MIR domain sitting above Pmt4-A, and the Pmt4-B MIR domain leaning toward Pmt4-A. Second, the Pmt4 MIR domain has an extended loop in the MIR motif 1 that interacts with the acceptor peptide, to be described below (Fig. 1c). The TMD contains the donor dolichol-P-Man-binding site. Above the TMD and facing the ER lumen resides the catalytic pocket comprised of luminal TMH-connecting loops, including two short horizontal α -helices (HH1 and HH2) connecting TMH1 and TMH2, and two additional horizontal α -helices (HH3a/b and HH4) and a two-stranded β -sheet (S1 and S2) connecting TMH7 and TMH8 (Fig. 1c, e). Below the TMD-facing cytosol are the N-terminal short α -helix and short TMH-connecting loops. This small section maintains Pmt4 dimerization, which is important for Pmt4 activity.

Unlike the Pmt1–Pmt2 dimer interface that is largely stabilized by the N-terminal β -hairpin of Pmt1³², the Pmt4 dimer is stabilized in both cytosolic and luminal regions but with minimal contacts in the TMD region (Fig. 1f). The luminal contact is mediated by the ends of the two TMH9s, involving two L656 residues of the two protomers, as well as two ordered lipid molecules. The cytosolic interface involves Pmt4-B W260 π -stacking with Pmt4-A H622, and Pmt4-B L263 and D264 interacting with Pmt4-A H622. There is a 20-Å cavity in the dimer believed to facilitate the diffusion of the membrane-embedded Dol-P-Man into either one of the two catalytic pockets.

Acceptor and donor binding in the TMD catalytic pocket

The yeast cell wall protein 5 (Ccw5) was previously shown to be a good Pmt4 substrate²⁹. Therefore, we synthesized an S/T-rich (50%) peptide of Ccw5 (108-ASKTSTNATSSCATPSLKD-127) as a model acceptor and used Man-1-P as a donor mimic to understand how the acceptor substrate protein is selectively recognized by Pmt4. Cryo-EM analysis yielded two 3D EM maps: a binary Pmt4–Ccw5 complex at 3.2 Å resolution and a ternary Pmt4–Ccw5–man complex at 3.5 Å resolution (Supplementary Figs. 1d, 3).

The 3D map of Pmt4–Ccw5 contains densities for both Ccw5 peptide (Fig. 2a, b) and Dol in the TMD cavity, and the location of Dol is

similar to that of Dol-P in Pmt1–Pmt2³². The thin and zigzagged density in the Pmt4 map lacks the phosphate moiety. We presume the phosphate is disordered and therefore modeled a dolichol in the donor EM density. The hydrophobic dolichol chain resides in an extended groove between TMH10 and TMH11 and is stabilized by hydrophobic side chains of V245 and V256 of TMH10 and F278, L282, and V286 of TMH11.

Surprisingly, the Ccw5 peptide interacts with two separate regions of the Pmt4 dimer, with the N-terminal segment (N-segment) being sandwiched between the two MIR domains and the C-terminal segment (C-segment) interacting with the catalytic pocket of Pmt4-A (Fig. 2d–f). The two MIR domains both move toward the center to interact with the N-segment of the Ccw5 peptide (Fig. 2d, Supplementary Fig. 4a–d). Compared to the apo Pmt1 structure, the Pmt4-B MIR domain is rotated 16° and shifted 36 Å toward Pmt4-A, and the Pmt4-A MIR domain is rotated 15° and shifted down by 16 Å (Fig. 2d, Supplementary Figs. 5 and 6). These movements enabled the two MIR domains to sandwich and interact with the Ccw5 peptide. The side-by-side arrangement of the two MIR domains may have evolved to facilitate substrate-peptide trapping and threading. The primary substrate interaction is mediated by the two MIR motif loops of the Pmt4-B MIR domain (Fig. 2e). However, the local resolution is too low to identify the peptide sequence in this region, due to the partial mobility of these MIR domains. This problem is remediated by our additional crystallographic study, to be described below.

The peptide C-segment fits snugly in a shallow groove near the catalytic pocket of Pmt4-A (Fig. 2f). This groove has a surface area of 370 Å², is lined by HH1, HH3, HH4, S1, and S2 and their connecting loops (Supplementary Fig. 7), and stabilizes a 10-residue region of the Ccw5 C-segment (116-TSSCATPSL-125). The HH1 residues F79, D80, H83, and N759 near S1 and S2, and the HH4 residues H563 and L559 interact with the Ccw5 C-segment (Fig. 2f). Therefore, both the MIR domain and the catalytic pocket contribute to the acceptor substrate selection.

The substrate-binding groove in the TMD region is important for Pmt4 function

Using a structure-based homology sequence alignment server (Dali)³⁷, we compared the acceptor binding grooves of all seven *S. cerevisiae* PMT family members Pmt1–7 and found that all acceptor binding grooves contain three horizontal α -helices (HH1–3) and an intervening loop (Fig. 2g). HH1–3 are arranged similarly across the family, but the intervening loops vary: the loop is 9–10 residues long in Pmt1, 4, and 5, and is 12–13 residues in Pmt2, 3, 6, and 7. The longer intervening loops make the acceptor binding grooves larger. The 80-DE-81 dipeptide is conserved and essential for Pmt activity³⁸. Six additional residues are also well conserved: H83, L559, H563, F662, F313, and N759. To examine their functional importance, we generated three double mutations: H83A/H563A, L559A/F662A, and F313A/N759A, and purified the WT and mutant Pmt4 enzymes (Supplementary Fig. 8). We examined their ability to hydrolyze Man-1-P in the presence of the 20-residue Ccw5 peptide acceptor. In this assay, free phosphate released from Man-P is detected by the Biomol Green reagent. We found that the peptide acceptor drastically stimulated the WT Pmt4 activity but not the H83A/H563A and F313A/N759A double mutant activity (Fig. 2h), indicating that these regions are crucial for proper enzymatic function. In contrast, the L559A/F662A mutation did not affect the Pmt4 activity, suggesting this region may be less critical for peptide binding or function.

Pmt4 MIR domain recognizes a S/T-X-S/T motif of an acceptor substrate

As mentioned above, the side chains of the Ccw5 peptide were not resolved in the binding N-segment with the Pmt4-B MIR domain. To address this ambiguity, we expressed the Pmt4 MIR domain in *E. coli*, co-crystallized it with the same 20-residue Ccw5 peptide that was used

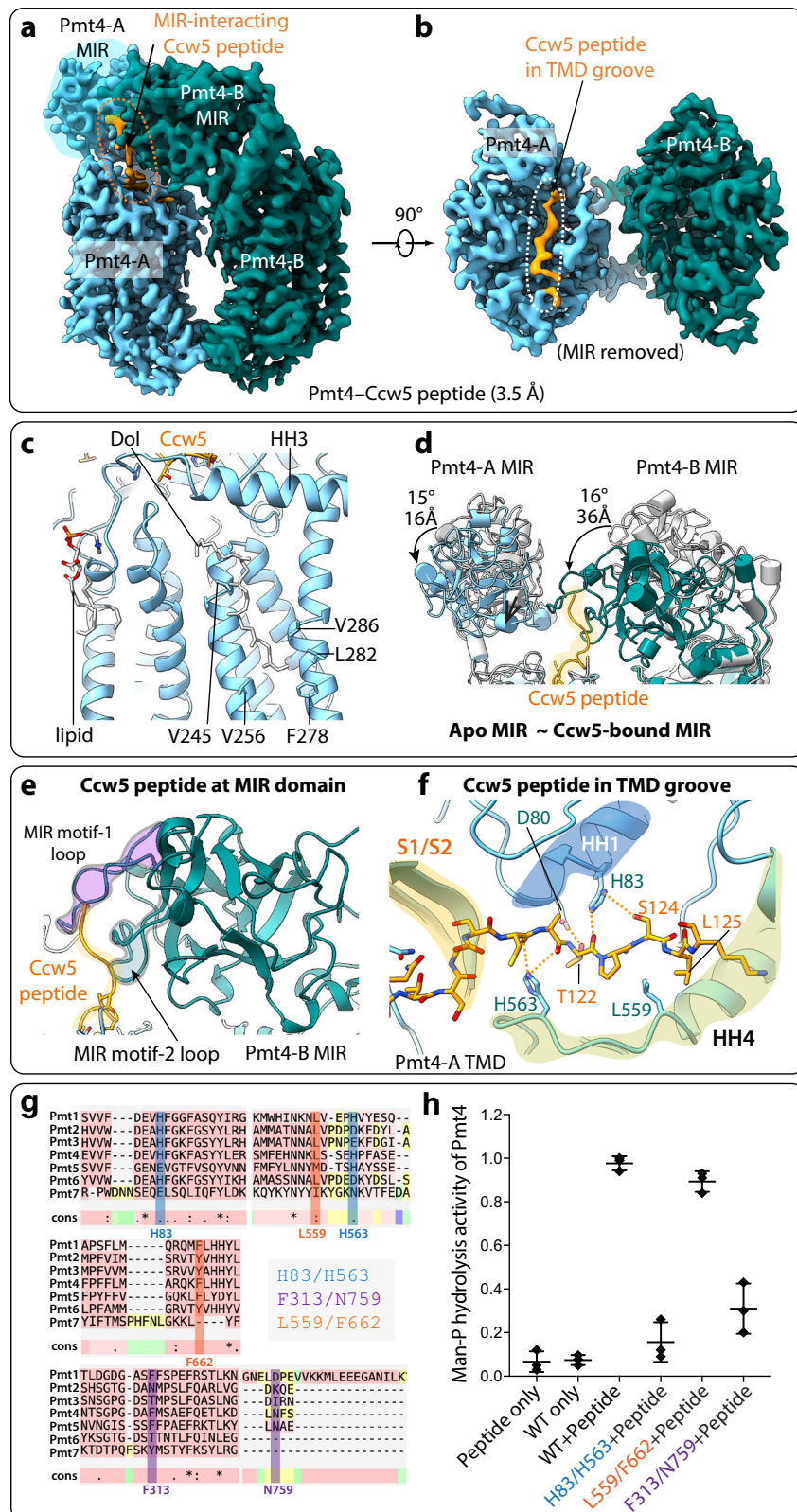


Fig. 2 | The Pmt4–Ccw5 peptide binary complex. Cryo-EM map processed by EMReady in a side (a) and top view (b). The MIR domains are removed in the top view to show the peptide density in the TMD groove. Pmt4-A is in cyan, and Pmt4-B is in teal. **c** A lipid and a dolichol bind in the transmembrane domain (TMD). **d** The MIR domains rotate and shift to bind the Ccw5 peptide. **e** Pmt4-B MIR motif loops 1–2 bind the Ccw5 peptide. **f** Ccw5 peptide in the peptide-binding groove of Pmt4-A. **g** Sequence alignment of *S. cerevisiae* Pmt1–7 in the peptide-binding groove. The

six conserved groove residues are highlighted and combined into three doublets for double mutations: H83/H563, F313/N759, and L559/F662. **h** Phosphate release activity was assessed by incubating the Ccw5 peptide with purified WT or mutant Pmt4 proteins in the presence of Man-P. Control assays were performed with the peptide alone and the Pmt4 alone. Mean \pm SD of three independent experiments, with all data points displayed as solid circles. Source data are provided as a Source Data file.

in the cryo-EM study (Supplementary Fig. 9), and solved the co-crystal structure at a resolution of 1.69 Å (Fig. 3a–d, Supplementary Table 2). We found that one asymmetric unit contains three copies of the MIR domain and identified two distinct binding modes between the MIR domain and the Ccw5 peptide. Specifically, two MIR domains each bind a TST motif, and the remaining MIR domain binds a TSS motif in the Ccw5 N-segment (109-SKTSTNATSSS-119) (Fig. 3a–d). In both binding modes, the same loops from the MIR-1 and MIR-2 motifs engage with the S/T-rich regions of the peptide, i.e., 111-Thr-Ser-Thr-113 and 117-Thr-Ser-Ser-119 (Fig. 3d).

In the TST binding mode, the Ccw5 T111 forms two hydrogen bonds with I367 in the MIR-1 loop and one hydrogen bond with A425 in the MIR-2 loop. T113 forms one hydrogen bond with D423 of the MIR-2 loop and one hydrogen bond with K507 of the MIR-3 loop (Fig. 3b). N114, immediately following the TST motif, also forms a hydrogen bond with P430. The TSS binding mode is highly similar to the TST binding mode: T116 forms two hydrogen bonds with the MIR domain, and S118 forms one hydrogen bond with D423 and one hydrogen bond with K507 in the MIR-3 loop (Fig. 3d, e). Notably, the middle S112 in the TST binding mode and the middle S117 in the TSS binding mode are both oriented away from the MIR domain and do not participate in the substrate-enzyme interaction (Fig. 3d, e). Therefore, we suggest that the central residue in the tripeptide motifs is inconsequential and propose that the Pmt4 MIR domain recognizes an S/T-X-S/T motif. The recognition mode may account for Pmt4's preference for acceptor substrates with multiple S/T-rich regions³¹.

Remarkably, the co-crystal structure of Pmt4 MIR domain–Ccw5 peptide fits very well as a rigid body into the cryo-EM density of the acceptor peptide (Fig. 3f). This enabled us to build a hybrid model for the stabilized 17-residue region of the 20-residue Ccw5 peptide in the EM map, including the rigid-body docked N-terminal six residues interacting with the Pmt4 MIR domain, and the C-terminal 11 residues situated above the TMD in and around the Pmt4's catalytic pocket. This unique spatial arrangement suggests that the MIR domain may recognize the S/T-X-S/T motif on Ccw5 and guide the acceptor to the catalytic site for mannosylation. While the S/T-X-S/T alone is rather nonspecific, the enzyme's detection of the coincidence of two such motifs (the other being the acceptor S/T site) likely increases the substrate specificity.

To investigate the importance of the MIR motif loops interacting with the S/T-X-S/T motif, we introduced two mutations in the Pmt4 MIR: either by shortening the MIR-1 motif loop by seven residues ($\Delta 362-368$) or by swapping a 9-residue region of the MIR-2 motif loop with a poly-alanine peptide of the same length (423–431>Ala). The mutant Pmt4 MIR domains were produced in *E. coli* and purified for isothermal titration calorimetry (ITC) assay (Supplementary Fig. 9). The WT Pmt4 MIR domain bound the 20-residue Ccw5 peptide with a dissociation constant (K_D) of $12 \pm 0.9 \mu\text{M}$. However, the two mutations largely abolished the MIR domain's binding capacity to the substrate peptide (Fig. 3g, Supplementary Fig. 10). This result underscores the importance of the observed S/T-X-S/T recognition mechanism by the Pmt4 MIR domain.

The MIR domain peptide-binding site is distinct from the proposed Man-binding site

The MIR domains of Pmt2 and Pmt3 were previously found to have low mM affinity for Man, and it was suggested that the Pmt2 MIR domain contains four potential Man-binding sites (α , β , γ , and δ) and the Pmt3 MIR domain one site (α)³³ (Fig. 4a, b). We aligned the current structure of the Pmt4 MIR–Ccw5 complex with the structures of the Pmt2 MIR (PDB 6ZQP) and Pmt3 MIR domains (PDB 6ZQQ) and found that the Ccw5 peptide-binding site is extended and spans the triangular surface of the Pmt4 MIR domain (Fig. 4c, d). Therefore, the substrate-peptide-binding site is distinct from and has no overlaps with the proposed Man-binding sites, which are at the sides of the triangular Pmt2 and Pmt3 MIR domains. However, the side chains of Ser-112 are oriented

such that a covalently linked Man might be positioned toward and occupy the proposed Man-binding site β (Fig. 4c). Therefore, in addition to recognizing unmodified substrate peptides, we speculate the Pmt MIR domain may play a secondary role in binding mannosylated peptide products.

Pmt4–Ccw5–Man structure and the mannose transfer mechanism

As mentioned above, we obtained a 3.5-Å resolution 3D map of the Pmt4–Ccw5 peptide–Man ternary complex (Supplementary Fig. 3). In this map, an isolated planar density was observed about 2.5 Å below the acceptor residue T122 of the Ccw5 peptide (Fig. 5a), and we assigned this density as mannose that was likely derived from hydrolysis of the donor mimic Man-1-P added to the cryo-EM sample. A thin and zigzag density was also present in the donor Dol-P-Man-binding groove, but only dolichol region can be modeled because the density lacked the phosphate moiety (Supplementary Fig. 3c). The lack of phosphate density in our EM maps is likely due to the steric conflict of the two phosphate moieties, one from Man-1-P and the other from the endogenous donor product dolichol-P co-purified with the enzyme, leading to their displacement and therefore, the lack of their densities. Therefore, our modeling of the Dol is tentative, and future studies using alternative donor analogs or time-resolved cryo-EM may be required to capture the intact donor-bound state.

Next, we computationally aligned the published Pmt1-2 structure with the Pmt4–Ccw5–Man ternary structure and found that the phosphate moiety of Dol-P in Pmt1-2 is ~2.4 Å further below the observed mannose in the Pmt4 structure, apparently suitable for covalent bond formation with Man (Fig. 5b, c). The predicted phosphate site is suitably coordinated by five positively charged residues, H101, K241, R659, H664, and H665 (Fig. 5c, Supplementary Fig. 6a–d). Therefore, the observed Pmt4–Ccw5–Man structure is likely in a post-mannosylation state, in which the phosphate has been released, and the Man has been transferred to the accepting T122, which is stabilized by H83 and H563. The structure is consistent with the S_N2 inverting transfer mechanism, in which the nearby D80 first deprotonates the -OH group of the acceptor T122, which goes on to nucleophilically attack the mannose anomeric C1, leading to the covalent attachment of the Man to T122 and glycosyl transfer (Fig. 5d). Because the phosphate is below Man C1, and T122 is above C1, the new β -linkage between T122 and Man is an inversion of the α -linkage between Man and phosphate in the donor, consistent with the inverting transfer mechanism. Although this mechanism is supported by structural alignment and chemical reasoning, it remains speculative and requires further validation by targeted mutagenesis and visualization of additional reaction intermediates.

Dual acceptor recognition and the dimeric PMT architecture

The Ccw5 peptide binding in the ternary Pmt4–Ccw5–Man structure is similar to that described above in the binary Pmt4–Ccw5 structure (Figs. 2e, f, 4c, d). If we label the *O*-mannosylated T122 as position 0, the residues N-terminal to T122 will have negative position numbers, and residues C-terminal to T122 will have positive position numbers. The substrate groove at position 0 is lined by H83 and H563 that sandwich T122, apparently stabilizing the residue for accepting the mannose moiety (Fig. 6a). We showed above that, although they are not catalytic, these two His residues are essential to Pmt4 function (Fig. 2h). However, the MIR domain binding site at positions -9 to -11 (S/T-X-S/T) is about 10 residues upstream of the accepting T122. Therefore, the interaction between Pmt4 and Ccw5 involves two sites in the substrate. We suggest that this dual-site recognition is the mechanism Pmt4 has evolved to ensure modification on highly S/T-enriched regions.

All PMT family members form dimers—either heterodimers or homodimers—and dimerization is required for their function, even though individual PMT proteins contain both acceptor and donor

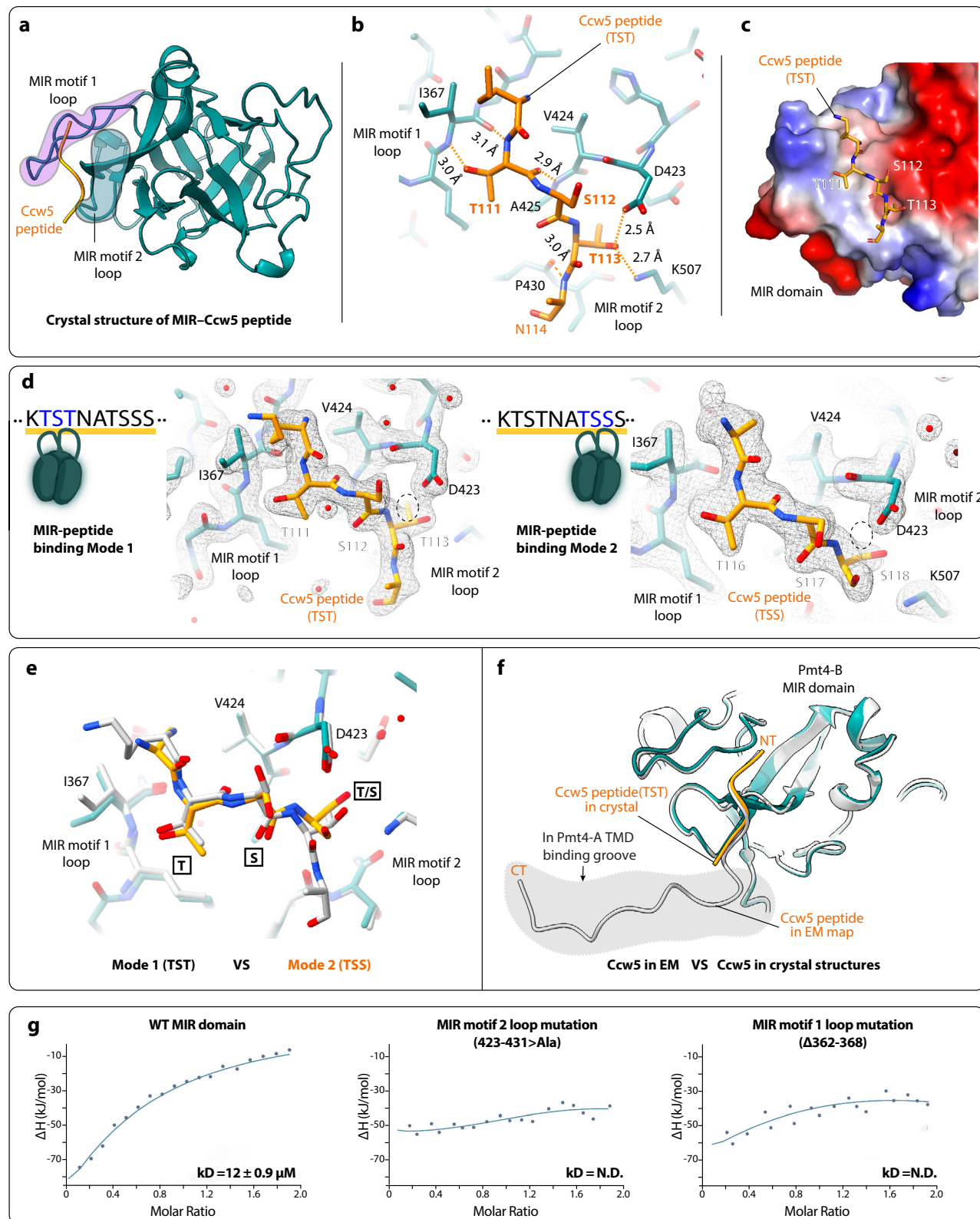


Fig. 3 | Co-crystal structure of MIR domain-Ccw5 peptide complex. **a** Cartoon view of the co-crystal structure of the MIR-Ccw5 peptide complex. **b** Detailed interactions of the Ccw5 peptide with the Pmt4 MIR domain. **c** The MIR domain is shown in surface charge, and the Ccw5 peptide in sticks. **d** Two MIR-Ccw5 peptide-binding modes, in which the bound Ccw5 peptides in sticks are superimposed with the electron density in gray meshes. Created in BioRender. <https://BioRender.com/>

e Superimposition of two crystal structures of the MIR domain-Ccw5 peptide complex (Model 1 in gray and Model 2 in color). **f** Superimposition of cryo-EM (gray) and crystal (color) structures of the MIR domain-Ccw5 peptide complex. **g** Fittings of ITC titration of WT Pmt4 MIR (left), MIR motif 2 loop mutant (423-432>Ala, middle), and MIR motif 1 loop mutant (Δ 362-368). The mutant Pmt4 MIR domains had little affinity for the Ccw5 peptide.

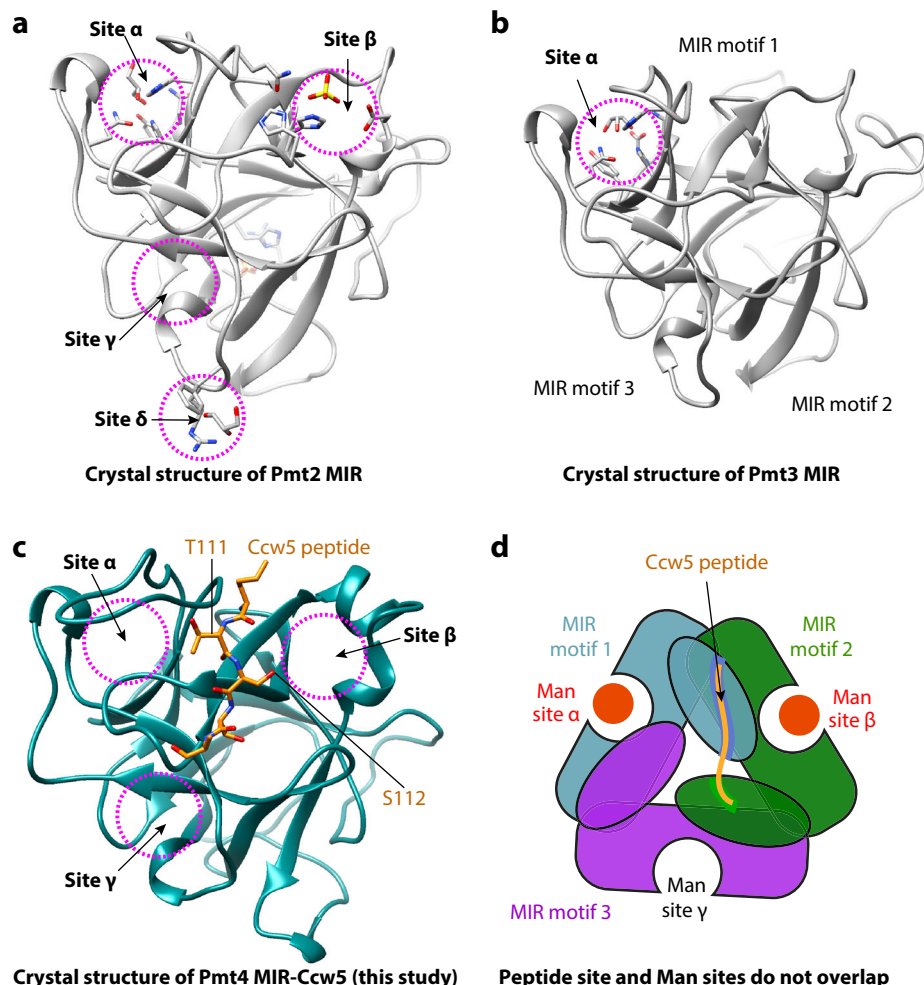


Fig. 4 | Comparison of previously suggested MIR domain Man-binding sites with the observed Ccw5 peptide-binding site in Pmt4. Suggested Man-binding sites α , β , γ , and δ in the crystal structures of the Pmt2 MIR domain (PDB ID 6ZQP, **a**) and Man-binding site α in the Pmt3 MIR domain (PDB 6ZQQ, **b**). **c** The Ccw5 peptide

in the Pmt4 MIR domain. The three dashed magenta circles indicate Man sites α , β , and γ in the Pmt2 MIR. **d** Sketch showing that the previously suggested Man-binding sites do not overlap with the observed substrate-peptide-binding site in the Pmt4 MIR domain. The red circle represents the Mannose molecules.

binding sites⁴. This raises an intriguing question about the underlying biological reason. We have elucidated Pmt4's strategy for recognizing and binding acceptor proteins. Our cryo-EM analysis of the Pmt4 dimer under saturating Ccw5 peptide has revealed that each Pmt4 protomer contains two peptide-binding sites. However, the peptide is bound at two separate locations in trans, with the first site containing an S/T-X-S/T motif that is recognized by the MIR domain of Pmt4-B, and the second site about 10 residues downstream containing the Man-accepting residue S/T. This second peptide site is recognized by a groove above the TMD of Pmt4-A (Fig. 6b). Therefore, the recruitment of a single Ccw5 peptide requires both Pmt4 protomers. We suggest that such a trans-dual-site recognition mechanism is the underlying reason for the conserved dimeric architecture, whether a homodimer or a heterodimer. Finally, based on the previously reported mannose binding by the MIR domains³³, the MIR domains may also function in mannosylated product substrate threading, as indicated by the purple dots on the substrate peptides (Fig. 6b).

Methods

Pmt4 protein expression and purification

The *pmt4* gene was amplified from the yeast genome DNA and cloned into the integrated and galactose-inducible vector pRSII403 with a C-terminal 3xFLAG tag. All constructs were verified by sequencing. The pRSII403-Pmt4 plasmid was transformed into yeast strain W303(MATa

leu2-3,112 trp1-1 can1-100 ura3-1 ade2-1 his3-11) for protein overexpression. The yeast cells were grown in SD growth medium w/o HIS before being inoculated into 18 L of the YPG medium (1% yeast extract, 2% peptone, 2% glycerol) at 30 °C. When cell density reached OD₆₀₀ = 1.0, galactose (2% w/v) was added to induce Pmt4 overexpression for about 6 h at 30 °C. The cells were harvested by 4000 × g centrifugation, then the pellet was resuspended in the lysis buffer (20 mM Tris, pH 7.5, 200 mM Sorbitol, 300.0 mM CH₃COOK, 2.0 mM EDTA) supplemented with protease inhibitor cocktail (1.0 mM phenylmethylsulphonyl fluoride, 2 mM pepstatin, 0.8 μM aprotinin, and 2.0 μg/mL leupeptin). The suspensions were frozen into "yeast popcorn" in liquid nitrogen, and the cells were pulverized using a freezer mill (SPEX CertiPrep 6850 Freezer Mill). The yeast powder was slowly thawed in a cold room, and insoluble material was removed by centrifugation at 4000 × g for 10 min. The yeast membranes containing Pmt4 were pelleted by ultracentrifugation at 125,440 × g for 1 h. The membrane pellet was solubilized by gentle mixing in a cold room for 1 h in the lysis buffer plus 1% w/v DDM. The detergent-solubilized membrane was centrifuged at 100,000 × g for 45 min, and the supernatant containing detergent-solubilized Pmt4 was incubated with anti-FLAG affinity resin (GenScript) at 4 °C for 2 h. Pmt4 was eluted by Flag peptide (0.2 mg/ml) in the elution buffer (20 mM Tris, pH 7.5, 150 mM NaCl, 1.0 mM MgCl₂, 1.0 mM MnCl₂, 1.0 mM CaCl₂, 0.005% LMNG, 0.0005% CHS). The eluent was further separated by size exclusion

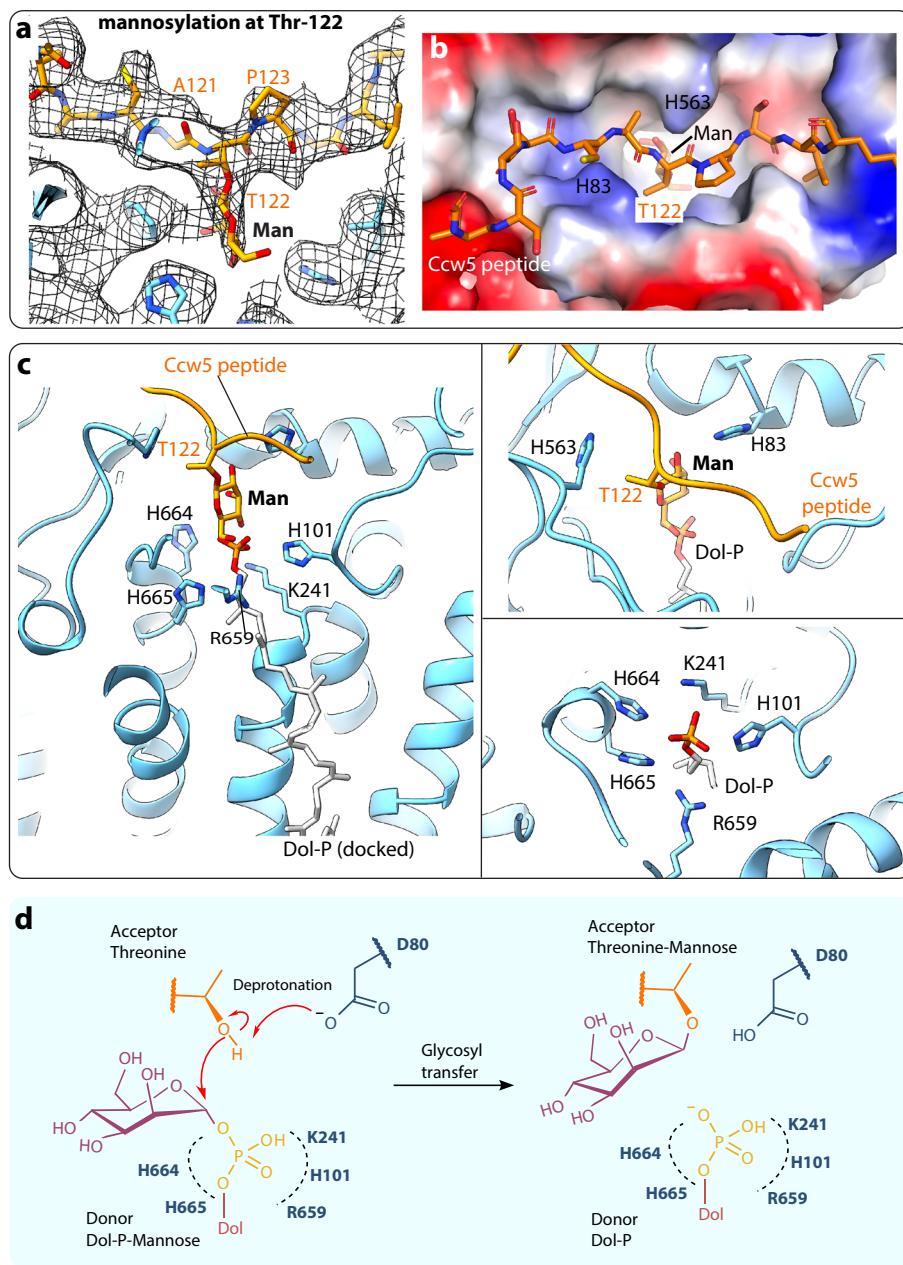


Fig. 5 | Cryo-EM structure of the ternary Pmt4–Ccw5–Man complex. **a** Atomic model and density map around the catalytic pocket showing covalently linked Man to T122. **b** Surface charge view of the substrate-binding groove and catalytic pocket in Pmt4. **c** Structure of the Pmt4–Ccw5–Man with computationally docked Dol-P.

The two right panels show H563 and H83 lining the substrate-binding groove near the acceptor T122 (upper) and five residues in the donor binding pocket coordinating the phosphate of the docked Dol-P (lower). **d** Proposed catalytic mechanism. See text for details.

chromatography (Superose 6 10/300 GL column, GE Healthcare) in the elution buffer. The gel filtration fractions were analyzed by SDS-PAGE, and the fractions containing Pmt4 were pooled, concentrated to 2.4 mg/ml, and stored.

Three Pmt4 mutants, H83A/H563A, L559A/F662A, and F313A/N759A, were cloned, expressed, and purified using the same protocol as for the wild-type Pmt4 protein. Each mutant was concentrated to approximately 2.0 mg/ml and stored accordingly for the subsequent activity assay. We did not attempt cryo-EM structural analysis on these mutant Pmt4 proteins.

Expression and purification of wild-type and mutant forms of the Pmt4 MIR domain

The PCR products corresponding to the MIR domain of Pmt4 (amino acids 330–521) were cloned into the pSUMO expression vector.

Expression was carried out in *Escherichia coli* BL21 (DE3), producing an N-terminal 6×His-SUMO fusion protein. The bacterial cultures were grown in LB medium at 30 °C until the OD₆₀₀ reached 0.8, followed by induction with 0.05 mM IPTG at 16 °C overnight. Initial purification involved Ni-affinity chromatography using a buffer containing 20 mM Tris (pH 7.5), 200 mM NaCl, and 10% glycerol, with elution in the same buffer supplemented with 300 mM imidazole. The 6×His-SUMO tag was subsequently cleaved using Ulp1 protease, and the cleaved protein was re-bound to a nickel HP column. Final purification was achieved via gel filtration chromatography (Superdex 75 10/300) in a buffer containing 20 mM Tris (pH 7.5) and 200 mM NaCl. Two Pmt4 MIR domain mutants, the MIR motif loop 2 mutant (423–432>Ala) and the MIR motif loop 1 deletion mutant (Δ362–368), were produced following similar protocols (Supplementary Figs. 9 and 10).

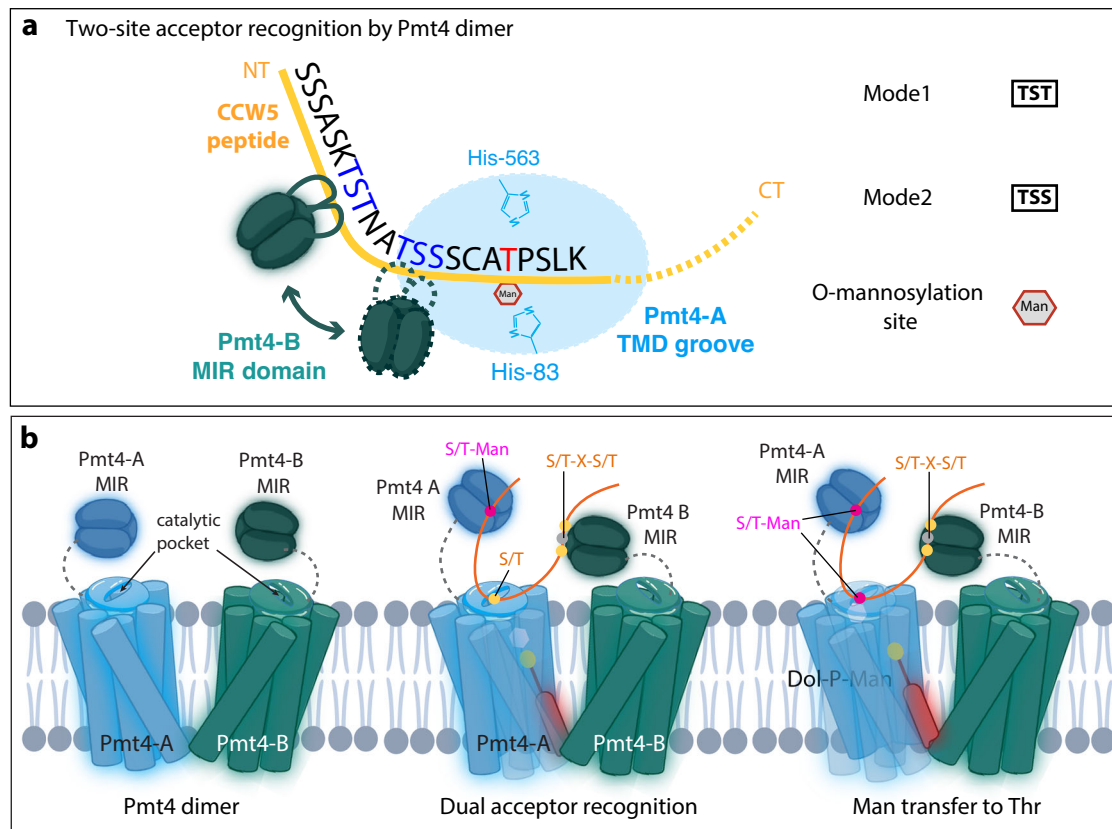


Fig. 6 | Proposed dual substrate recognition by Pmt4. **a** Dual-site acceptor recognition model of Pmt4. T122 at position 0 (catalytic site) is the mannose-accepting residue. The MIR domain of Pmt4-B interacts with two S/T at positions -9 and -11 , and the Pmt4-A substrate-binding groove, including H83 and H563, recognizes and positions the accepting S/T at position 0 for *O*-mannosylation. Created in BioRender. <https://BioRender.com/k41037m>. **b** Like all PMT family members, Pmt4 maintains a dimer architecture via interactions at both luminal and cytosolic regions. The MIR domains are mobile. An S/T-rich acceptor peptide is recognized at two locations that are about 10 residues apart. The peptide-binding

groove above the transmembrane domain of one Pmt4 binds a peptide segment containing the accepting S/T, and the MIR domain of the other Pmt4 binds the S/T-X-S/T region of the substrate peptide, ensuring only the S/R-rich region of a protein substrate can be modified. Such a two-site *trans*-binding mode may explain the invariable and essential dimer architecture of all PMT enzymes. Because the MIR domain can bind mannose, it is possible that the MIR domain plays a dual function of selecting the substrate peptide (yellow dots) and facilitating the threading of mannosylated product peptide (purple dots). Created in BioRender. <https://BioRender.com/k41037m>.

Crystallization, data collection, and structure determination

Crystallization screen for the purified MIR domain alone and the MIR domain–Ccw5 complex was conducted using the sitting-drop vapor diffusion method at 20 °C. Crystals of the MIR domain alone emerged in 3 days from drops comprising 0.1 μ l of a protein solution at 10.0 mg/ml and 0.1 μ l of a reservoir solution containing 1.0 M LiCl, 0.1 M citric acid, and 30% PEG 6000 (w/v) at pH 8.0. Crystals of the MIR domain–Ccw5 peptide complex also appeared in 3 days from drops containing 0.1 μ l of a MIR domain at 10.0 mg/ml mixed with Ccw5 peptide at 1:1.5 molar ratio and 0.1 μ l of a reservoir solution containing 25% polyethylene glycol monomethyl ether 2000 at pH 8.0 (Supplementary Fig. 11). The crystals were harvested by flash freezing by liquid nitrogen in 15% glycerol. X-ray diffraction datasets were collected at the Life Sciences Collaborative Access Team (LS-CAT) beamlines at the Argonne National Laboratory, at 100 K with an X-ray wavelength of 1.078 Å. Diffraction data were processed in HKL-2000³⁹. Initial phasing was determined by the molecular replacement method in the PHENIX program⁴⁰, using our previously published EM structure of the Pmt1 MIR domain (PDB ID 6P2R) as the search model. Subsequent manual model adjustments and rebuilding were done in Coot⁴¹. Further refinement of the manually built model was carried out using Refmac in the CCP4 suite⁴² and PHENIX⁴³. Several iterations of real-space manual adjustment and reciprocal refinement led to the final R_{work} of 19.0% and R_{free} of 22.7% for the MIR domain model, and the final R_{work} of

18.4% and R_{free} of 20.8% for the MIR domain–Ccw5 model (Supplementary Table 2).

Cryo-EM

Purified full-length Pmt4 was mixed with the 20-residue Ccw5 peptide (108-ASKTSTNATSSCATPSLK-127) at a molar ratio of 1:10 to form the enzyme–acceptor peptide complex. Man-1-P of 5 mg/ml was subsequently added to the mixture of Pmt4 and Ccw5 peptide to form the ternary enzyme–acceptor–donor complex. To prepare cryo-EM grids, we applied a 2.0- μ l droplet of either the purified Pmt4 or the above-described ternary mixture to glow-discharged C-flat 2/1 holey carbon grids held by a pair of tweezers in an FEI Vitrobot (mark IV) with the sample chamber environment set to 6 °C and 95% humidity and incubated for 10.0 s before blotting for 3.0 s, then plunging the grids into liquid-nitrogen-cooled liquid ethane. The grids were stored in a liquid nitrogen dewar. Pmt4 particles frozen on the C-flat 2/1 grids were well distributed with no aggregation problem. We collected a cryo-EM dataset semi-automatically by SerialEM⁴⁴ in a Titan Krios electron microscope operated at a high tension of 300 kV. Micrographs were recorded at a nominal scope magnification of $\times 130,000$ and a defocus range from -1.5 to -2.5 μ m in a Gatan K3 direct electron detector operated at the super-resolution mode. A Gatan BioQuantum energy filter installed in front of the K3 detector was used in zero-energy-loss mode with an energy slit of 20.0 eV to remove inelastically scattered electrons and improve image contrast. At the used

magnification, each detector pixel corresponds to 0.828 \AA at the sample level. The exposure dose rate was 10.0 electrons per \AA^2 per second, and the exposure time for each 30-frame movie micrograph was 6.0 s (i.e., 0.2 s per frame), leading to a total exposure dose of $60\text{ e}/\text{\AA}^2$.

Image processing and 3D reconstruction

We collected in TFS Titan Krios a dataset of 2010 raw movie micrographs for apo Pmt4. The movie frames were first aligned and superimposed by the program Motioncorr 2.0. The contrast transfer function parameters of each aligned micrograph were calculated using the program CTFFIND4⁴⁵. All the remaining steps, including particle auto selection, 2D classification, 3D classification, 3D refinement, and density map post-processing, were performed using Relion-4.0⁴⁶. The template for automatic picking was generated from a 2D average of about ~10,000 manually picked particles in different views. Automatic particle selection was performed for the entire dataset, and 192,368 particles were initially picked. We then carefully inspected the selected particles, removed “bad” ones, re-picked some initially missed “good” ones, and sorted the remaining good particles by similarity to the 2D references, in which the bottom 10% of particles with the lowest z-scores were removed from the particle pool. 2D classification of all good particles was performed, and particles in the classes with unrecognizable features by visual inspection were removed. A total of 92,548 particles were used for further 3D classification. We derived five 3D models from the dataset and chose the best model for the final refinement, in which classes 3–5 were combined for further refinement. The final datasets have 45,052 particles. They were used for further 3D refinement, resulting in 3.9 \AA 3D density maps. The resolution of each map was estimated by the gold-standard Fourier shell correlation, at the correlation cutoff value of 0.143. The final map was sharpened by applying a negative B-factor of -172 \AA^2 .

We next collected in a TFS Titan Krios a dataset of 7033 raw movie micrographs for the ternary mixture of Pmt4, Ccw5 peptide, and Man-1-P. Using a similar data processing approach as with the Pmt4 apo sample, we auto-picked 492,368 particles and carried out 2D and 3D classification and 3D refinement. This resulted in a 3D map at 3.2 \AA for the binary Pmt4–Ccw5 complex and another at 3.5 \AA for the ternary Pmt4–Ccw5–Man complex. The resolutions of these 3D maps were estimated by the gold-standard Fourier shell correlation with a correlation cutoff value of 0.143. The 3.2 \AA and 3.5 \AA density maps underwent sharpening through the application of negative B-factors of -177 \AA^2 and -163 \AA^2 , respectively.

Atomic modeling, refinement, and validation

For apo Pmt4 modeling, the model of the Pmt4 was initially built using the Swiss model online server (<https://swissmodel.expasy.org/>), and the resultant model was then manually updated in COOT⁴¹, guided by residues with bulky side chains like Arg, Phe, Tyr, and Trp. The two MIR domains were shifted and docked into the corresponding density. For Pmt4–Ccw5 and Pmt4–Ccw5–Man modeling, the above-described apo Pmt4 model was first docked as a rigid body into the EM maps. The MIR domains were shifted separately as rigid bodies into the EM map. With the sequence information of the Ccw5 peptide, a 17-residue peptide model was built de novo into the density map. These two models were then refined by rigid-body refinement of individual chains in the PHENIX program⁴⁷, and subsequently adjusted manually in COOT. Finally, the atomic models were validated using MolProbity⁴⁸. Structural figures were prepared in Chimera⁴⁹ and Pymol (<https://www.pymol.org>).

Pmt4 activity assay

Three double mutant Pmt4 proteins, H83A/H563A, F313A/N759A, and L559A/F662A, were purified using the same procedures as for wild-type Pmt4. To perform the activity tests, 1 ml of buffer (25 mM HEPES,

pH 7.4; 50 mM NaCl, 5.0 mM MgCl₂, 0.005% LMNG, and 0.0005% CHS) was prepared. Recombinant proteins and Ccw5 peptide were added to 40 μl assay buffer and incubated in a 96-well plate for 5 min. The final protein concentrations were: Pmt4 WT or mutations (-1.5 μM), and Ccw5 peptide (2.0 μM). 45 μl of Man-1-P was added at a final concentration of 100 μM to begin the reactions. After 35 min at room temperature, reactions were stopped with 50 μl of BIOMOL Green reagent (Enzo Life Sciences). Absorbance at 635 nm was measured after 15 min and the relative activity was calculated. Reactions were performed in duplicates and repeated three times.

Isothermal titration calorimetry

Isothermal titration calorimetry (ITC) was performed to determine the interaction between the MIR domain mutant and the Ccw5 peptide. Two mutant MIR domains were expressed in *E. coli* and purified. The ITC studies were performed using a Nano ITC LV (190 μL) (TA Instruments, New Castle, DE) at 4 °C. A 190 μL solution of 100 μM WT or mutant MIR domain in buffer with 10 mM HEPES (pH 7.5), 100 mM NaCl, and 0.005% (v/v) Tween-20 was added to the sample cell. The Ccw5 peptide used for cryo-EM at 1.0 mM in 50 μL buffer solution was put into the instrument’s syringe. After achieving temperature equilibrium, 25 injections of 2- μL droplets of peptide were used for titration. The ITC data was then entered into the NanoAnalyze software (TA Instruments, New Castle, DE). After correcting the titration baseline, the ΔH and K_D values for MIR-peptide binding were calculated using the software. Three independent experiments were conducted.

Reporting summary

Further information on research design is available in the Nature Portfolio Reporting Summary linked to this article.

Data availability

The 3D cryo-EM maps of *S. cerevisiae* apo Pmt4 at 3.9 \AA , the binary Pmt4–Ccw5 complex at 3.2 \AA , and the ternary Pmt4–Ccw5–Man complex at 3.5 \AA have been deposited in the EMDB under accession codes EMD-47541, EMD-47566, EMD-47601, respectively. Their corresponding atomic models have been deposited in the Protein Data Bank under accession codes 9E61, 9E61, and 9E6V, respectively. The crystal structures of the Pmt4 MIR domain and the MIR domain–Ccw5 peptide complex were deposited in the RCSB PDB with accession codes 9E79 and 9E7A. Source data are provided with this paper.

References

1. Critcher, M., O’Leary, T. & Huang, M. L. Glycoengineering: scratching the surface. *Biochem. J.* **478**, 703–719 (2021).
2. Schjoldager, K. T., Narimatsu, Y., Joshi, H. J. & Clausen, H. Global view of human protein glycosylation pathways and functions. *Nat. Rev. Mol. Cell Biol.* **21**, 729–749 (2020).
3. Burda, P. & Aebi, M. The dolichol pathway of N-linked glycosylation. *Biochim. Biophys. Acta* **1426**, 239–257 (1999).
4. Loibl, M. & Strahl, S. Protein O-mannosylation: what we have learned from baker’s yeast. *Biochim. Biophys. Acta* **1833**, 2438–2446 (2013).
5. Lairson, L. L., Henrissat, B., Davies, G. J. & Withers, S. G. Glycosyltransferases: structures, functions, and mechanisms. *Annu. Rev. Biochem.* **77**, 521–555 (2008).
6. Pedersen, L. C. et al. Crystal structure of an alpha 1,4-N-acetylhexosaminyltransferase (EXTL2), a member of the exostosin gene family involved in heparan sulfate biosynthesis. *J. Biol. Chem.* **278**, 14420–14428 (2003).
7. Albesa-Jove, D., Giganti, D., Jackson, M., Alzari, P. M. & Guerin, M. E. Structure-function relationships of membrane-associated GT-B glycosyltransferases. *Glycobiology* **24**, 108–124 (2014).
8. Haltiwanger, R. S. & Lowe, J. B. Role of glycosylation in development. *Annu. Rev. Biochem.* **73**, 491–537 (2004).

9. Pradeep, P., Kang, H. & Lee, B. Glycosylation and behavioral symptoms in neurological disorders. *Transl. Psychiatry* **13**, 154 (2023).
10. Bausewein, D., Engel, J., Jank, T., Schoedl, M. & Strahl, S. Functional similarities between the protein O-mannosyltransferases Pmt4 from Bakers' yeast and human POMT1. *J. Biol. Chem.* **291**, 18006–18015 (2016).
11. Willer, T., Valero, M. C., Tanner, W., Cruces, J. & Strahl, S. O-mannosyl glycans: from yeast to novel associations with human disease. *Curr. Opin. Struct. Biol.* **13**, 621–630 (2003).
12. Carvalho, S. et al. O-mannosylation and N-glycosylation: two coordinated mechanisms regulating the tumour suppressor functions of E-cadherin in cancer. *Oncotarget* **7**, 65231–65246 (2016).
13. Imperiali, M. et al. O Mannosylation of alpha-dystroglycan is essential for lymphocytic choriomeningitis virus receptor function. *J. Virol.* **79**, 14297–14308 (2005).
14. Eisenhaber, B. et al. Conserved sequence motifs in human TMTC1, TMTC2, TMTC3, and TMTC4, new O-mannosyltransferases from the GT-C/PMT clan, are rationalized as ligand binding sites. *Biol. Direct* **16**, 4 (2021).
15. Larsen, I. S. B., Narimatsu, Y., Clausen, H., Joshi, H. J. & Halim, A. Multiple distinct O-Mannosylation pathways in eukaryotes. *Curr. Opin. Struct. Biol.* **56**, 171–178 (2019).
16. Bloch, J. S. et al. Structure, sequon recognition and mechanism of tryptophan C-mannosyltransferase. *Nat. Chem. Biol.* **19**, 575–584 (2023).
17. Crine, S. L. & Acharya, K. R. Molecular basis of C-mannosylation - a structural perspective. *FEBS J.* **289**, 7670–7687 (2022).
18. Bohl, H., Bai, L. & Li, H. Recent progress in structural studies on the GT-C superfamily of protein glycosyltransferases. *Subcell. Biochem* **96**, 259–271 (2021).
19. Alexander, J. A. N. & Locher, K. P. Emerging structural insights into C-type glycosyltransferases. *Curr. Opin. Struct. Biol.* **79**, 102547 (2023).
20. Olson, G. M., Fox, D. S., Wang, P., Alspaugh, J. A. & Buchanan, K. L. Role of protein O-mannosyltransferase Pmt4 in the morphogenesis and virulence of *Cryptococcus neoformans*. *Eukaryot. Cell* **6**, 222–234 (2007).
21. Plaza, V. et al. Botrytis cinerea PMT4 is involved in O-glycosylation, cell wall organization, membrane integrity, and virulence. *J. Fungi* <https://doi.org/10.3390/jof11010071> (2025).
22. Fernandez-Alvarez, A., Elias-Villalobos, A. & Ibeas, J. I. T. heO. -mannosyltransferase PMT4 is essential for normal appressorium formation and penetration in *Ustilago maydis*. *Plant Cell* **21**, 3397–3412 (2009).
23. Fernandez-Alvarez, A. et al. Identification of O-mannosylated virulence factors in *Ustilago maydis*. *PLoS Pathog.* **8**, e1002563 (2012).
24. Bai, L., Wang, T., Zhao, G., Kovach, A. & Li, H. The atomic structure of a eukaryotic oligosaccharyltransferase complex. *Nature* **555**, 328–333 (2018).
25. Ramirez, A. S., Kowal, J. & Locher, K. P. Cryo-electron microscopy structures of human oligosaccharyltransferase complexes OST-A and OST-B. *Science* **366**, 1372–1375 (2019).
26. Cherepanova, N., Shrimal, S. & Gilmore, R. N-linked glycosylation and homeostasis of the endoplasmic reticulum. *Curr. Opin. Cell Biol.* **41**, 57–65 (2016).
27. Gentzsch, M. & Tanner, W. The PMT gene family: protein O-glycosylation in *Saccharomyces cerevisiae* is vital. *EMBO J.* **15**, 5752–5759 (1996).
28. Gentzsch, M. & Tanner, W. Protein-O-glycosylation in yeast: protein-specific mannosyltransferases. *Glycobiology* **7**, 481–486 (1997).
29. Ecker, M. et al. O-mannosylation precedes and potentially controls the N-glycosylation of a yeast cell wall glycoprotein. *EMBO Rep.* **4**, 628–632 (2003).
30. Girrbach, V. & Strahl, S. Members of the evolutionarily conserved PMT family of protein O-mannosyltransferases form distinct protein complexes among themselves. *J. Biol. Chem.* **278**, 12554–12562 (2003).
31. Proszynski, T. J., Simons, K. & Bagnat, M. O. -glycosylation as a sorting determinant for cell surface delivery in yeast. *Mol. Biol. Cell* **15**, 1533–1543 (2004).
32. Bai, L., Kovach, A., You, Q., Kenny, A. & Li, H. Structure of the eukaryotic protein O-mannosyltransferase Pmt1-Pmt2 complex. *Nat. Struct. Mol. Biol.* **26**, 704–711 (2019).
33. Chiapparino, A. et al. Functional implications of MIR domains in protein O-mannosylation. *eLife* <https://doi.org/10.7554/eLife.61189> (2020).
34. Hutzler, J., Schmid, M., Bernard, T., Henrissat, B. & Strahl, S. Membrane association is a determinant for substrate recognition by PMT4 protein O-mannosyltransferases. *Proc. Natl. Acad. Sci. USA* **104**, 7827–7832 (2007).
35. Larsen, I. S. B. et al. Discovery of an O-mannosylation pathway selectively serving cadherins and protocadherins. *Proc. Natl. Acad. Sci. USA* **114**, 11163–11168 (2017).
36. Neubert, P. et al. Mapping the O-mannose glycoproteome in *Saccharomyces cerevisiae*. *Mol. Cell Proteom.* **15**, 1323–1337 (2016).
37. Holm, L., Laiho, A., Toronen, P. & Salgado, M. DALI shines a light on remote homologs: one hundred discoveries. *Protein Sci.* **32**, e4519 (2023).
38. Lommel, M., Schott, A., Jank, T., Hofmann, V. & Strahl, S. A conserved acidic motif is crucial for enzymatic activity of protein O-mannosyltransferases. *J. Biol. Chem.* **286**, 39768–39775 (2011).
39. Minor, W., Cymborowski, M., Otwinowski, Z. & Chruszcz, M. HKL-3000: the integration of data reduction and structure solution-from diffraction images to an initial model in minutes. *Acta Crystallogr. D Biol. Crystallogr.* **62**, 859–866 (2006).
40. Adams, P. D. et al. The Phenix software for automated determination of macromolecular structures. *Methods* **55**, 94–106 (2011).
41. Emsley, P., Lohkamp, B., Scott, W. G. & Cowtan, K. Features and development of Coot. *Acta Crystallogr. D Biol. Crystallogr.* **66**, 486–501 (2010).
42. Aguirre, J. et al. The CCP4 suite: integrative software for macromolecular crystallography. *Acta Crystallogr. D Struct. Biol.* **79**, 449–461 (2023).
43. Liebschner, D. et al. Macromolecular structure determination using X-rays, neutrons and electrons: recent developments in Phenix. *Acta Crystallogr. D Struct. Biol.* **75**, 861–877 (2019).
44. Mastronarde, D. N. Automated electron microscope tomography using robust prediction of specimen movements. *J. Struct. Biol.* **152**, 36–51 (2005).
45. Rohou, A. & Grigorieff, N. CTFFIND4: fast and accurate defocus estimation from electron micrographs. *J. Struct. Biol.* **192**, 216–221 (2015).
46. Scheres, S. H. RELION: implementation of a Bayesian approach to cryo-EM structure determination. *J. Struct. Biol.* **180**, 519–530 (2012).
47. Adams, P. D. et al. PHENIX: a comprehensive Python-based system for macromolecular structure solution. *Acta Crystallogr. D Biol. Crystallogr.* **66**, 213–221 (2010).
48. Chen, V. B. et al. MolProbity: all-atom structure validation for macromolecular crystallography. *Acta Crystallogr. D Biol. Crystallogr.* **66**, 12–21 (2010).
49. Pettersen, E. F. et al. UCSF Chimera-a visualization system for exploratory research and analysis. *J. Comput. Chem.* **25**, 1605–1612 (2004).

Acknowledgements

Cryo-EM data were collected at the David Van Andel Advanced Cryo-Electron Microscopy Suite at the Van Andel Institute. We thank G. Zhao

and X. Meng for their help with data collection. X-ray diffraction data was collected at the Lilly Research Laboratories Collaborative Access Team (LRL-CAT) at the Advanced Photon Source, which is a U.S. Department of Energy (DOE) Office of Science user facility operated for the DOE Office of Science by Argonne National Laboratory under Contract No. DE-AC02-06CH11357. This study was supported by the US National Institutes of Health grant CA231466 (to H.L.) and the Van Andel Institute (H.L.).

Author contributions

M.D., Z.Y., and H.L. conceived and designed experiments. M.D. made all constructs, cultured cells, purified proteins, and performed all biochemical and biophysical assays. M.D. collected cryo-EM and X-ray diffraction datasets. M.D. and Z.Y. solved the crystal structures, performed image processing, 3D reconstruction, and atomic modeling. A.K. and M.L. participated in sample preparations and biochemical assays. M.D., Z.Y., and H.L. analyzed the data and wrote the manuscript. All authors edited the manuscript.

Competing interests

The authors declare no competing interests.

Additional information

Supplementary information The online version contains supplementary material available at <https://doi.org/10.1038/s41467-025-64729-9>.

Correspondence and requests for materials should be addressed to Huilin Li.

Peer review information *Nature Communications* thanks Rouslan Efremov and the other anonymous reviewer for their contribution to the peer review of this work. A peer review file is available.

Reprints and permissions information is available at <http://www.nature.com/reprints>

Publisher's note Springer Nature remains neutral with regard to jurisdictional claims in published maps and institutional affiliations.

Open Access This article is licensed under a Creative Commons Attribution-NonCommercial-NoDerivatives 4.0 International License, which permits any non-commercial use, sharing, distribution and reproduction in any medium or format, as long as you give appropriate credit to the original author(s) and the source, provide a link to the Creative Commons licence, and indicate if you modified the licensed material. You do not have permission under this licence to share adapted material derived from this article or parts of it. The images or other third party material in this article are included in the article's Creative Commons licence, unless indicated otherwise in a credit line to the material. If material is not included in the article's Creative Commons licence and your intended use is not permitted by statutory regulation or exceeds the permitted use, you will need to obtain permission directly from the copyright holder. To view a copy of this licence, visit <http://creativecommons.org/licenses/by-nc-nd/4.0/>.

© The Author(s) 2025